

Targeted chemical pressure yields tuneable millimetre-wave dielectric

Natalie M. Dawley^{1,8}, Eric J. Marks^{2,3,8}, Aaron M. Hagerstrom³, Gerhard H. Olsen⁴, Megan E. Holtz^{1,4}, Veronica Goian⁵, Christelle Kadlec⁵, Jingshu Zhang¹, Xifeng Lu⁶, Jasper A. Drisko^{1,3}, Reinhard Uecker⁶, Steffen Ganschow⁶, Christian J. Long³, James C. Booth³, Stanislav Kamba⁵, Craig J. Fennie⁴, David A. Muller⁴, Nathan D. Orloff³ and Darrell G. Schlom^{1,7,*}

Epitaxial strain can unlock enhanced properties in oxide materials, but restricts substrate choice and maximum film thickness, above which lattice relaxation and property degradation occur. Here we employ a chemical alternative to epitaxial strain by providing targeted chemical pressure, distinct from random doping, to induce a ferroelectric instability with the strategic introduction of barium into today's best millimetre-wave tuneable dielectric, the epitaxially strained 50-nm-thick $n = 6$ $(\text{SrTiO}_3)_{n-1}(\text{BaTiO}_3)_1\text{SrO}$ Ruddlesden-Popper dielectric grown on (110) DyScO_3 . The defect mitigating nature of $(\text{SrTiO}_3)_{n-1}(\text{BaTiO}_3)_1\text{SrO}$ results in unprecedented low loss at frequencies up to 125 GHz. No barium-containing Ruddlesden-Popper titanates are known, but the resulting atomically engineered superlattice material, $(\text{SrTiO}_3)_{n-1}(\text{BaTiO}_3)_1\text{SrO}$, enables low-loss, tuneable dielectric properties to be achieved with lower epitaxial strain and a 200% improvement in the figure of merit at commercially relevant millimetre-wave frequencies. As tuneable dielectrics are key constituents of emerging millimetre-wave high-frequency devices in telecommunications, our findings could lead to higher performance adaptive and reconfigurable electronics at these frequencies.

The BaTiO_3 and SrTiO_3 material systems have long been studied for their tuneable dielectric and agile radio properties in the form of $(\text{Ba},\text{Sr})\text{TiO}_3$ (refs. ¹⁻⁵). $(\text{Ba},\text{Sr})\text{TiO}_3$ is an established compound that has use in the development of tuneable dielectrics and agile radio. In part, the popularity of $(\text{Ba},\text{Sr})\text{TiO}_3$ is due to its ease of fabrication and the ability to manipulate its ferroelectric Curie temperature, T_C , through the $\text{Ba}:\text{Sr}$ ratio, spanning 403 K for BaTiO_3 to 0 K for SrTiO_3 . The properties of $(\text{Ba},\text{Sr})\text{TiO}_3$ are engineered with chemical pressure, where bonds can be lengthened by the partial substitution of larger isovalent ions (such as barium) in the ionic material (SrTiO_3). The tuneability in $(\text{Ba},\text{Sr})\text{TiO}_3$, strained $(\text{SrTiO}_3)_{n-1}(\text{BaTiO}_3)_1\text{SrO}$ and the compound explored in this article $(\text{SrTiO}_3)_{n-1}(\text{BaTiO}_3)_1\text{SrO}$ (Fig. 1a) arises from the dipole created from the titanium–oxygen bonds in the paraelectric state of the ferroelectric materials; the titanium–oxygen bonds can be reversibly altered through an applied electric field, tuning the permittivity. With temperature, the highest tuneability is found when the titanium–oxygen interatomic potential well is widest, occurring just above the ferroelectric Curie temperature, T_C (ref. ¹). Unfortunately, even when used in the paraelectric state to reduce losses from domain wall motion and other loss mechanisms, dielectric losses increase as frequencies approach the millimetre-wave regime. Charged point defects in $(\text{Ba},\text{Sr})\text{TiO}_3$ thin films are one source of this increase in loss^{1,2,6}. In response, materials scientists are exploring concepts in materials design to control millimetre-wave losses.

Limitations of epitaxial strain

Previously⁷, we showed that the $(\text{SrTiO}_3)_{n-1}(\text{BaTiO}_3)_1\text{SrO}$ Ruddlesden-Popper superlattices^{8,9} formed by inserting layers of $(\text{SrO})_2$ into strained SrTiO_3 led to defect mitigation and lower dielectric loss¹⁰⁻¹²,

precipitating the highest recorded figure of merit (FOM) for all known tuneable millimetre-wave dielectrics. Although this work built an understanding of how to control losses in ferroelectrics, film thicknesses were limited to 50 nm and below. Above 50 nm the highly strained film began to relax, and the electrical properties degraded. Expansion of the available parameters for strain engineering beyond the limits of epitaxial strain¹³⁻¹⁶ would facilitate the synthesis of these high-performance tuneable dielectrics on common commercial substrates, such as sapphire, MgO or LaAlO_3 , and allow films to be grown thicker to maximize device tuneability, while maintaining low loss. In millimetre-wave electronics, many planar circuit geometries rely on the interaction of electric fields generated in a circuit device patterned on an adjacent tuneable dielectric film. For films with thicknesses on the order of nanometres, most of the field does not interact with the tuneable film, but rather with the non-tuneable substrate and superstrate (see Supplementary Fig. 1). As a result, even if a device is patterned on a highly tuneable dielectric film, the overall device tuneability can be minimal for thin films. The ability to grow thicker films on cost-effective commercial substrates is essential for the practical implementation of tuneable dielectric materials in millimetre-wave electronics.

First-principles calculations of targeted chemical pressure

To guide our efforts to realize a thicker, more tuneable Ruddlesden-Popper dielectric material, the effect of epitaxial strain and chemical pressure on the ferroelectric polarization was investigated with first-principles calculations (see Methods section), to provide an indication of room-temperature electric-field tuneability. Polarization in these materials is a quantitative indicator of tuneability. The contribution of each atomic layer to the ferroelectric polarization

¹Department of Materials Science and Engineering, Cornell University, Ithaca, NY, USA. ²Department of Materials Science and Engineering, University of Maryland, College Park, MD, USA. ³National Institute of Standards and Technology, Boulder, CO, USA. ⁴School of Applied and Engineering Physics, Cornell University, Ithaca, NY, USA. ⁵Institute of Physics ASCR, Prague, Czech Republic. ⁶Leibniz-Institut für Kristallzüchtung, Berlin, Germany. ⁷Kavli Institute at Cornell for Nanoscale Science, Ithaca, NY, USA. ⁸These authors contributed equally: Natalie M. Dawley, Eric J. Marks. ^{*}e-mail: schlom@cornell.edu

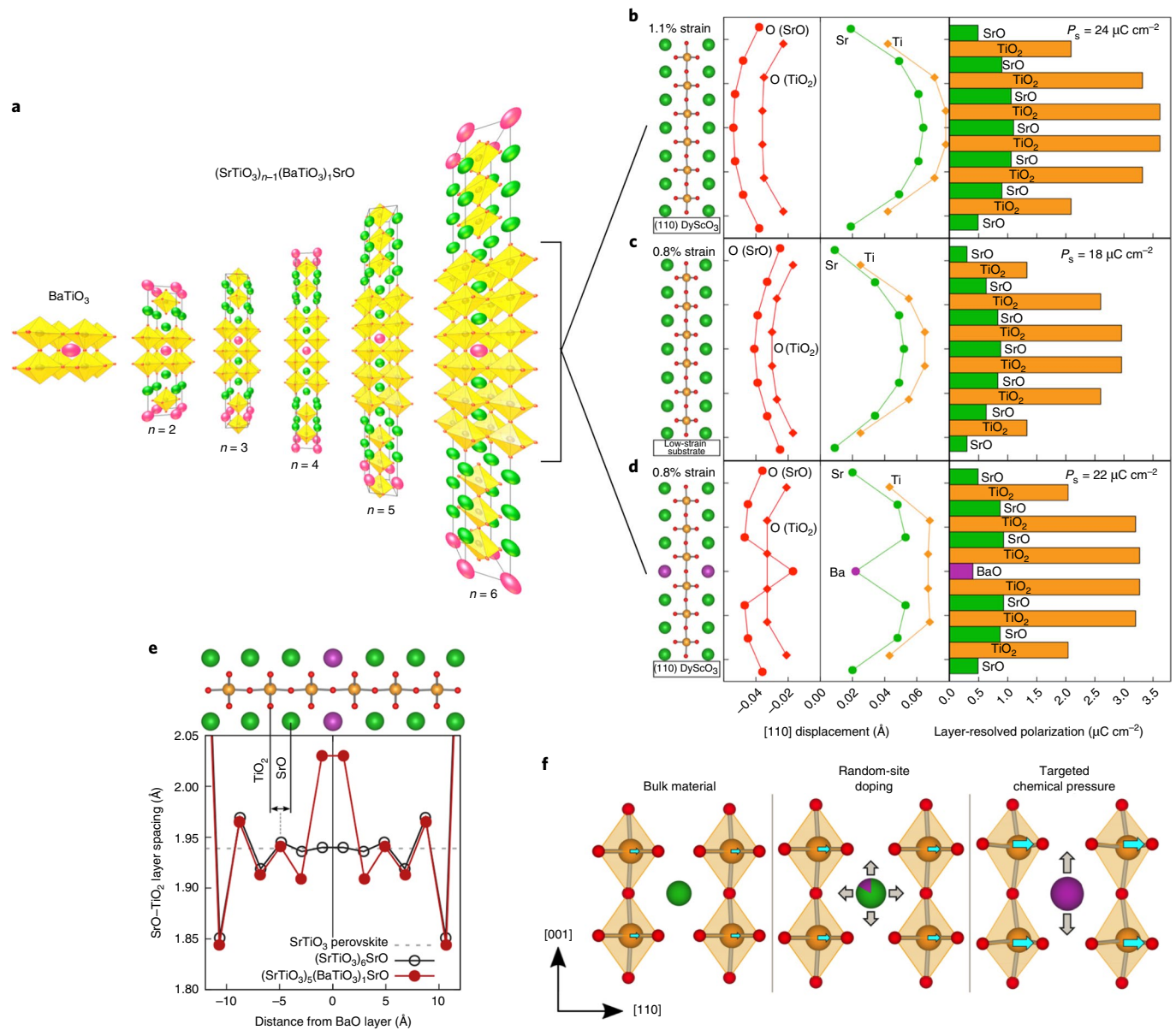


Fig. 1 | The inequivalence of local chemical and global epitaxial strain in $(\text{SrTiO}_3)_{n-1}(\text{BaTiO}_3)_n\text{SrO}$ phases. a, Crystal structure schematic of BaTiO_3 and the $n=2-6$ $(\text{SrTiO}_3)_{n-1}(\text{BaTiO}_3)_n\text{SrO}$ phases. Strontium atoms are shown in green, barium in pink and the unit cells are outlined. **b-d**, The effect of epitaxial strain and the addition of the larger barium atom from first-principles calculations on local in-plane ferroelectric polarization in the $n=6$ $(\text{SrTiO}_3)_{n-1}(\text{BaTiO}_3)_n\text{SrO}$ perovskite block of the Ruddlesden-Popper superlattice. Contribution to ferroelectric polarization throughout the $n=6$ $(\text{SrTiO}_3)_6\text{SrO}$ unit cell epitaxially strained to (110) DyScO_3 (**b**), $n=6$ $(\text{SrTiO}_3)_6\text{SrO}$ unit cell epitaxially strained to an intermediate epitaxial strain of 0.8% (**c**) and $n=6$ $(\text{SrTiO}_3)_{n-1}(\text{BaTiO}_3)_n\text{SrO}$ unit cell epitaxially strained to (110) DyScO_3 (**d**). Although **c** and **d** have the same epitaxial strain, the addition of the local strain from a single larger barium atom further increases the total ferroelectric polarization. **e**, The distortion of the atoms along the c axis from the addition of a single BaO layer. **f**, Schematic of how strain in the perovskite section of the epitaxial Ruddlesden-Popper superlattice, grey arrows, imposed by bulk chemical pressure via random doping of barium, middle illustration, differs from targeted chemical pressure, far right illustration. Random doping leads to an expansion around the barium in both in-plane and out-of-plane directions, whereas targeted chemical pressure, in which an entire layer is δ -doped with barium, leads to solely out-of-plane expansion. For the Ruddlesden-Popper superlattice under tensile strain, and out-of-plane ferroelectric polarization suppressed by the $(\text{SrO})_2$ layers, this local out-of-plane expansion manifests in an enhanced local in-plane polarization.

was calculated at 0 K for a range of strain and barium concentrations in a series of $n=6$ compounds (Fig. 1b-d and Supplementary Fig. 2a-d); the $n=6$ (SrTiO_3) _{n} SrO phase was found to be the optimal periodicity n in our previous work⁷. Figure 1b shows results of density functional theory (DFT) calculations for the current state-of-the-art $n=6$ (SrTiO_3) _{n} SrO films grown on (110)-oriented DyScO_3 for a 1.1% epitaxial strain. If we simply lower the epitaxial strain in (SrTiO_3) _{n} SrO from 1.1 to 0.8%, to enable the growth of thicker films

(Fig. 1c), a 25% reduction in spontaneous polarization is observed, demonstrating the drawback of relying solely on epitaxial strain to enable high tuneability. If the same state of 0.8% tensile strain is reached by substituting a single layer of barium into the superlattice (Fig. 1d), the polarization is reduced by only 8%. The barium layer itself does not enhance polarization, but instead strains the neighbouring TiO_2 and SrO layers, in turn leading to a net higher polarization. In Fig. 1e we show the spacing between each SrO and

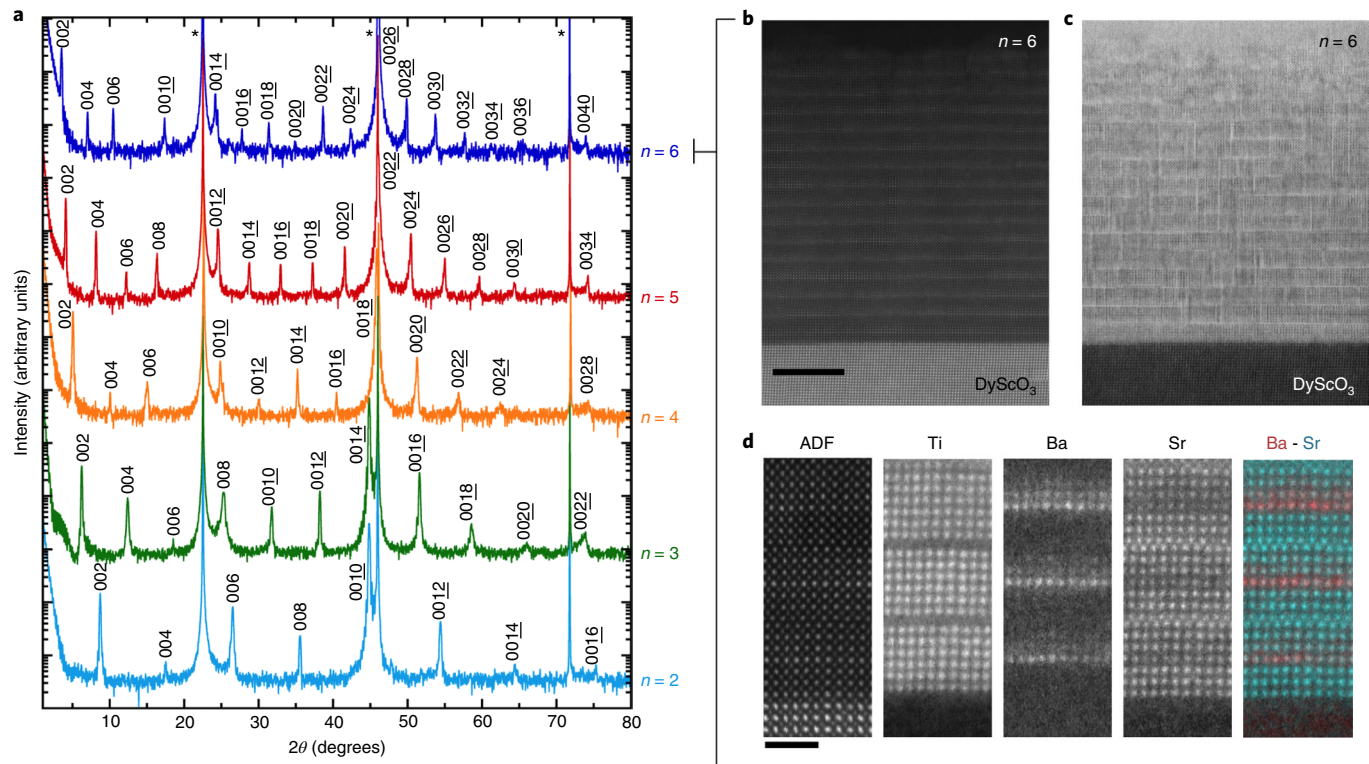


Fig. 2 | Structural characterization of ~50-nm-thick epitaxial $(\text{SrTiO}_3)_{n-1}(\text{BaTiO}_3)_1\text{SrO}$ films with $n = 2-6$ grown on (110) DyScO_3 substrates. **a**, θ - 2θ scans of the 50-nm-thick $n = 2-6$ $(\text{SrTiO}_3)_{n-1}(\text{BaTiO}_3)_1\text{SrO}$ films grown on (110) DyScO_3 . Substrate peaks are labelled with an asterisk. **b**, High-angle annular dark-field STEM image of the 50-nm-thick $n = 6$ sample whose X-ray diffraction is shown in dark blue in **a**. Scale bar, 10 nm. **c**, Bright-field STEM image of the same $n = 6$ film. **d**, ADF and STEM-EELS images of the same $n = 6$ region showing the elemental distributions from the $\text{Ti-}L_{2,3}$ edge, the $\text{Ba-}M_{4,5}$ edge and the $\text{Sr-}L_{2,3}$ edge, with a colour overlay of the barium signal in red and the strontium in teal. The barium shows one to two unit cells of interdiffusion to higher layers in the crystal structure; that is, in the direction of film growth. Scale bar, 2 nm.

TiO_2 layer as a function of the distance from the BaO layer in the middle of the perovskite block. The out-of-plane expansion of the TiO_2 layers from strain imposed by the larger barium atom-layer is confined to a few nearest-neighbour layers, demonstrating the importance of high-quality molecular-beam epitaxy (MBE) growth. The confinement of barium to an atomically thin layer thus sets up a local strain field which in turn creates a targeted chemical pressure, enhancing in-plane ferroelectric polarization as shown schematically in Fig. 1f. To corroborate this proposed mechanism, we also performed calculations where the virtual crystal approximation was used to simulate the effect of barium being randomly distributed within the perovskite block, such as the compound $(\text{Ba}_{0.2}\text{Sr}_{0.8}\text{TiO}_3)_5(\text{SrTiO}_3)_1\text{SrO}$ shown in Supplementary Fig. 2b. This systematically led to lower calculated polarizations, highlighting that precise layering of BaO is the optimal strategy for realizing low-loss tunable dielectric films with moderate epitaxial strains.

This effect that we are calling ‘targeted chemical pressure’ is a model proposed here to manipulate properties with strain at the local atomic level, beyond what can be achieved with bulk doping in chemical pressure. Targeted chemical pressure is the strain analogy to delta-doping of semiconductors, where a depth profile following a delta-function of dopants is grown in a semiconductor thin film to form a local charge carrier channel^{17,18}. Random-site doping for strain engineering, ‘chemical pressure’, exerts strain in all directions, suboptimal for the enhancement of an anisotropic property at the local atomic level in the Ruddlesden–Popper superlattice (Fig. 1f, middle). In an epitaxial film, the strain from targeted chemical pressure is constrained to the out-of-plane direction. In $(\text{SrTiO}_3)_{n-1}(\text{BaTiO}_3)_1\text{SrO}$ the targeted chemical pressure from the single barium layer in turn enhances the in-plane ferroelectricity of

the superlattice (Fig. 1f, right). This enhancement is due to the fact that out-of-plane ferroelectricity is suppressed in the Ruddlesden–Popper superlattice by the $(\text{SrO})_2$ planes that break up the Ti-O chains along the c axis to below the critical thickness required for ferroelectricity¹⁹. This leaves in-plane atomic displacements as the most favourable mechanism for relieving the local strain, which ultimately results in an increased polarization in the TiO_2 layers nearest and second-nearest to the BaO layer (Fig. 1d).

The local strain effect from the introduction of BaTiO_3 is distinct from previous reports of $(\text{BaTiO}_3)_m(\text{SrTiO}_3)_n$ superlattices where the polarization is in the out-of-plane direction and arises from the compressively strained BaTiO_3 polarizing neighbouring SrTiO_3 layers^{20,21}. In strained $(\text{SrTiO}_3)_n\text{SrO}$ and $(\text{SrTiO}_3)_{n-1}(\text{BaTiO}_3)_1\text{SrO}$, the polarization lies in the plane of the film and decreases near the $(\text{SrO})_2$ boundary where the perovskite unit cell shifts by $\frac{1}{2}a[110]$ breaking the ferroelectric titanium–oxygen chain¹⁹. In addition to enhancing polarization, confining the barium to a single layer far from the $(\text{SrO})_2$ shear planes is advantageous to minimize the likelihood of forming secondary phases. BaTiO_3 is metastable in the Ruddlesden–Popper structure, with the non-perovskite barium orthotitanate (Ba_2TiO_4) being the lowest energy phase^{22,23}; indeed no barium-containing Ruddlesden–Popper titanates are known to form in bulk and the $(\text{SrTiO}_3)_{n-1}(\text{BaTiO}_3)_1\text{SrO}$ phases that we have targeted lie in a two-phase region of the BaO-SrO-TiO_2 pseudoternary phase diagram²⁴. Nevertheless, as we show below, these artificial phases can be atomically engineered through oxide MBE.

Growth and characterization of $(\text{SrTiO}_3)_{n-1}(\text{BaTiO}_3)_1\text{SrO}$

To compare to our previous $(\text{SrTiO}_3)_n\text{SrO}$ work⁷, $n = 2-6$ films of $(\text{SrTiO}_3)_{n-1}(\text{BaTiO}_3)_1\text{SrO}$ with the same thickness, 50 nm, and on

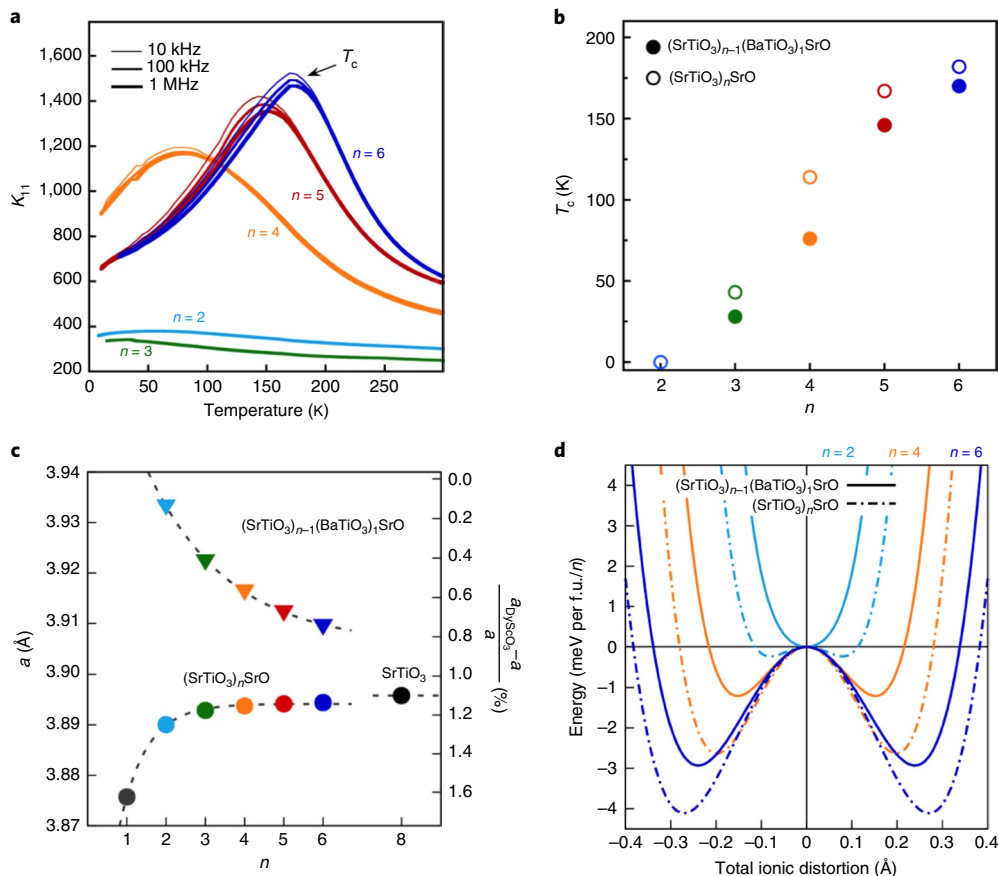


Fig. 3 | Emergence of ferroelectricity in $(\text{SrTiO}_3)_{n-1}(\text{BaTiO}_3)_1\text{SrO}$ films grown on (110) DyScO_3 . **a**, In-plane dielectric-constant (K_{11}) measurement as a function of temperature of the $n=2-6$ $(\text{SrTiO}_3)_{n-1}(\text{BaTiO}_3)_1\text{SrO}$ films that are about 50-nm-film thick and are grown on (110) DyScO_3 substrates. **b**, Comparison of the T_c of $(\text{SrTiO}_3)_{n-1}(\text{BaTiO}_3)_1\text{SrO}$ films taken from the peak in **a** at 10 kHz (closed circles) to $(\text{SrTiO}_3)_n\text{SrO}$ (open circles). **c,d**, First-principles calculations showing how the index n can be used to control the local ferroelectric instability of $(\text{SrTiO}_3)_{n-1}(\text{BaTiO}_3)_1\text{SrO}$ and $(\text{SrTiO}_3)_n\text{SrO}$ phases strained commensurately to (110) DyScO_3 substrates. Equilibrium lattice parameters in **c** are for the Ruddlesden-Popper compounds in the parent space group $I4/mmm$ (left axis), and the tensile strain imposed when they are grown on (110) DyScO_3 (right axis). Potential energy surfaces in **d** are for the in-plane polar distortion (space group $F2mm$) for the $n=2, 4, 6$ compounds with and without barium.

the same substrate, (110) DyScO_3 ($a_{\text{pseudocubic}} \approx 3.949 \text{ \AA}$)²⁵, were grown via MBE, along with a thicker (100 nm) $n=6$ film of $(\text{SrTiO}_3)_{n-1}(\text{BaTiO}_3)_1\text{SrO}$ on (110) DyScO_3 . The structural quality of the films is important to obtain the lowest loss devices and was examined using four-circle X-ray diffraction (Fig. 2a) and Supplementary Fig. 3). The films show clear periodicity in $\theta-2\theta$ scans, indicating they are single phase.

To investigate the placement of the metastable BaO layer in the $(\text{SrTiO}_3)_{n-1}(\text{BaTiO}_3)_1\text{SrO}$ phases, we used scanning transmission electron microscopy (STEM) and electron energy-loss spectroscopy (EELS) on a cross-sectional specimen projecting through a $\{100\}$ plane (Fig. 2b-d and Supplementary Figs. 4-6). It was found that barium had one to two unit cells of intermixing with the strontium layers above it. A brick-and-mortar-like structure of the Ruddlesden-Popper superlattice (Fig. 2d) was observed indicating the presence of $(\text{SrO})_2$ layers accommodating local non-stoichiometry. We did not observe any secondary phases, indicating that higher barium concentrations are probably possible in this artificial material; that is, $(\text{SrTiO}_3)_{n-m}(\text{BaTiO}_3)_m\text{SrO}$ phases with $m > 1$.

Ferroelectric properties

For electric-field tuneable dielectrics, the highest tuneability is found near the ferroelectric transition temperature, T_c , in the paraelectric phase of the material. To identify the T_c of these previously unexplored phases, the in-plane permittivity of the films was measured

as a function of temperature and frequency (Fig. 3a, see Methods). The peak in the in-plane dielectric-constant curve with temperature indicates the onset of ferroelectricity, T_c . By increasing n , the thickness of the perovskite repeat unit, the polar mode emerges and strengthens¹⁹, increasing T_c . The $(\text{SrTiO}_3)_{n-1}(\text{BaTiO}_3)_1\text{SrO}$ phases with $n=2-3$ show little ferroelectric behaviour while $(\text{SrTiO}_3)_{n-1}(\text{BaTiO}_3)_1\text{SrO}$ phases $n=4-6$ show relaxor ferroelectric behaviour (see ferroelectric hysteresis loops in Supplementary Fig. 7a) originating from the separation of the ferroelectric perovskite blocks by the $(\text{SrO})_2$ layers¹⁹. Compared to the pure $(\text{SrTiO}_3)_n\text{SrO}$ phase in Fig. 3b, the T_c of the $(\text{SrTiO}_3)_{n-1}(\text{BaTiO}_3)_1\text{SrO}$ phases are lower as explained by the first-principles calculations below.

The experimental trends in T_c are consistent with DFT calculations of the ferroelectric energy landscape (Fig. 3d). The depth of these double-well potentials, a representation of the internal energy at zero temperature, is often regarded as a proxy for the ferroelectric T_c . For each periodicity n , the potentials are shallower for barium-containing $(\text{SrTiO}_3)_{n-1}(\text{BaTiO}_3)_1\text{SrO}$ compounds than for the pure $(\text{SrTiO}_3)_n\text{SrO}$ materials when both films are grown on (110) DyScO_3 , reflecting the reduction of tensile strain from $\sim 1.1\text{--}1.6\%$ for $(\text{SrTiO}_3)_n\text{SrO}$ to $0.1\text{--}0.8\%$ for $(\text{SrTiO}_3)_{n-1}(\text{BaTiO}_3)_1\text{SrO}$ (dependent on n , see Fig. 3c). Despite the fact that $(\text{SrTiO}_3)_{n-1}(\text{BaTiO}_3)_1\text{SrO}$ has a lower epitaxial strain state it still maintains robust ferroelectric properties when compared to $(\text{SrTiO}_3)_n\text{SrO}$ at the same lower epitaxial strain state, as in Fig. 1c for 0.8% epitaxial strain (see also

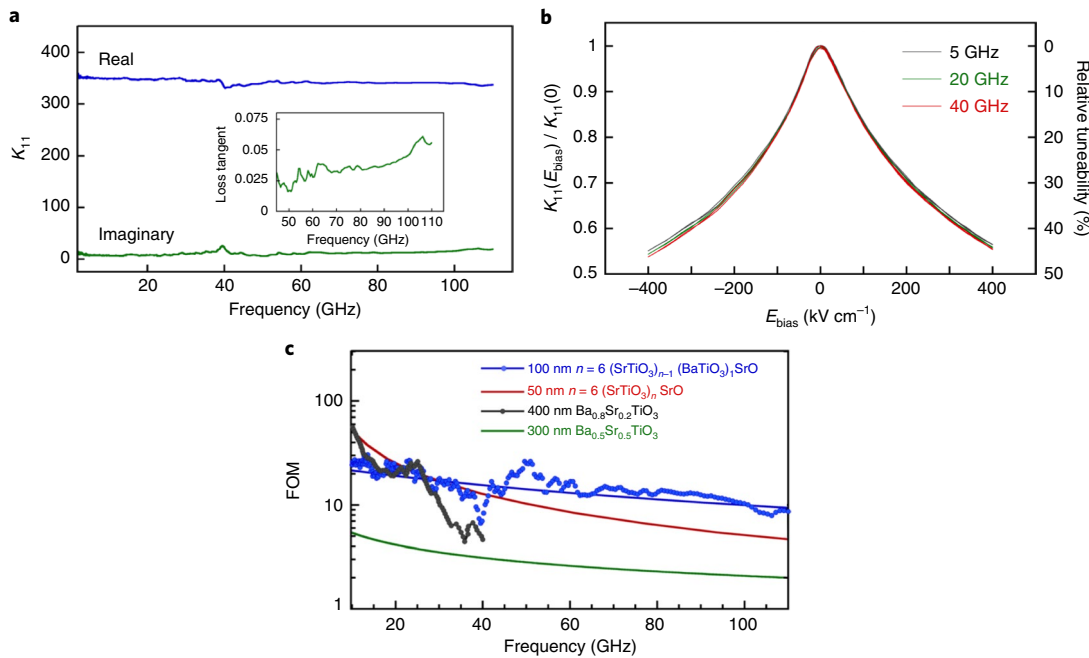


Fig. 4 | In-plane dielectric constant (K_{11}) of 100-nm $n=6$ (SrTiO_3) $_{n-1}$ (BaTiO_3) $_1$ SrO film on (110) DyScO_3 , and its tuneability at room temperature and high frequency. **a**, Real and imaginary parts of K_{11} as a function of frequency for the 100-nm-thick $n=6$ film. The inset shows the film loss tangent on a linear frequency scale in the microwave-frequency regime. **b**, The ratio of K_{11} under an applied bias field (E_{bias}) to $K_{11}(0)$ (left-hand axis) and relative tuneability (right-hand axis) of the $n=6$ sample at several different frequencies in the microwave range. **c**, Room-temperature FOM (blue) of the same 100-nm-thick $n=6$ sample ($E_{\text{bias}}=400 \text{ kV cm}^{-1}$), (red) of the 50-nm-thick $n=6$ (SrTiO_3) $_n$ SrO on (110) DyScO_3 sample ($E_{\text{bias}}=50 \text{ kV cm}^{-1}$) from ref. ¹², (grey) a $x=0.8$ $\text{Ba}_x\text{Sr}_{1-x}\text{TiO}_3$ film ($E_{\text{bias}}=500 \text{ kV cm}^{-1}$) from ref. ²⁸ and (green) a $x=0.5$ $\text{Ba}_x\text{Sr}_{1-x}\text{TiO}_3$ film ($E_{\text{bias}}=300 \text{ kV cm}^{-1}$) from ref. ²⁷. The FOM of the $n=6$ sample uses the measured loss tangent, but assumes the tuneability is independent of frequency and is 46% at $E_{\text{bias}}=400 \text{ kV cm}^{-1}$.

Fig. 3 and Supplementary Fig. 7b). These calculations indicate that targeted chemical pressure with the introduction of a single barium layer can provide thicker commensurate films with enhanced polarization beyond what can be achieved with ‘global’ strain methods such as epitaxial strain via substrate choice (as in Fig. 1c) or random-site doping (seen in Supplementary Fig. 2b).

Millimetre-wave performance

To test the applicability of our materials to next-generation millimetre-wave devices such as reconfigurable antennas, tuneable filters and phase shifters, we examined the complex permittivity from 600 Hz to 110 GHz (Methods) of a 100-nm-thick $n=6$ (SrTiO_3) $_{n-1}$ (BaTiO_3) $_1$ SrO sample at 300 K (Fig. 4a and Supplementary Fig. 9a). The absence of major dispersion in the measured range is analogous to the performance of the previously reported (SrTiO_3) $_n$ SrO films. The loss tangent (Fig. 4a inset) begins to increase in the millimetre-wave regime and reaches 0.06 at 110 GHz. Similar loss behaviour observed in the (SrTiO_3) $_n$ SrO materials was attributed to the presence of polar nanoregions with a finite distribution of sizes⁷. This behaviour is in contrast to the (Ba,Sr) TiO_3 system, which can display notable relaxation in the millimetre-wave regime. This relaxation is often attributed to the presence of charged point defects in addition to domain wall interactions and the aforementioned polar nanoregions. In Supplementary Fig. 10 we show a comparison of the dielectric constant of $n=6$ (SrTiO_3) $_{n-1}$ (BaTiO_3) $_1$ SrO and $\text{Ba}_x\text{Sr}_{1-x}\text{TiO}_3$ at terahertz frequencies and observe that our $n=6$ (SrTiO_3) $_{n-1}$ (BaTiO_3) $_1$ SrO material is superior in that it provides comparable loss to $\text{Ba}_x\text{Sr}_{1-x}\text{TiO}_3$ with low x , but that its soft mode is notably softer than that of $\text{Ba}_x\text{Sr}_{1-x}\text{TiO}_3$ with low x , resulting in higher tuneability and a higher FOM at millimetre-wave frequencies. The relatively low loss of our (SrTiO_3) $_{n-1}$ (BaTiO_3) $_1$ SrO films at millimetre-wave frequencies despite their similar chemical makeup to the (Ba,Sr) TiO_3 alloy system supports the idea that these films

maintain the defect mitigating nature of (SrTiO_3) $_n$ SrO Ruddlesden–Popper films.

Tuneability of the permittivity was measured by applying a quasi-static electric field to the 100-nm-thick (SrTiO_3) $_{n-1}$ (BaTiO_3) $_1$ SrO $n=6$ film. A maximum applied field of 400 kV cm^{-1} reduced the dielectric constant of the film by more than 46% (Fig. 4b). The applied field did not alter the frequency dependence of the permittivity and loss tangent in the measured range from 100 MHz to 40 GHz (Supplementary Fig. 9b,c).

By combining the two salient features of these materials, the tuneable dielectric FOM (Fig. 4c) provides a convenient basis for comparing performance²⁶. Another metric of comparing tuneable dielectrics, the commutation quality factor K parameter was measured up to 40 GHz and is shown in Supplementary Fig. 9d. This FOM multiplies the material quality factor, $Q=1/\tan\delta$, with the relative tuneability $(K_{11}(E_0) - K_{11}(E_{\text{max}}))/K_{11}(E_0)$ (Methods). E_0 represents no applied electric field and E_{max} represents the maximum applied electric field used to induce tuning. The outstanding room-temperature performance of the 100-nm $n=6$ (SrTiO_3) $_{n-1}$ (BaTiO_3) $_1$ SrO film at millimetre-wave frequencies is apparent, with a FOM of 25 at 10 GHz, and approximately 9 at 110 GHz, a 200% improvement on our previous FOM⁷. Figure 4c includes other results for comparison. These include our previous 50-nm $n=6$ (SrTiO_3) $_n$ SrO superlattice grown on (110) DyScO_3 ($E_{\text{max}}=50 \text{ kV cm}^{-1}$), a highly regarded result for a 300-nm-thick $\text{Ba}_{0.5}\text{Sr}_{0.5}\text{TiO}_3$ film on (0001) sapphire ($E_{\text{max}}=300 \text{ kV cm}^{-1}$)²⁷ and a recent report of a 400-nm-thick $\text{Ba}_{0.8}\text{Sr}_{0.2}\text{TiO}_3$ film in the ferroelectric manifold-domain-wall-variant state on (110) SmScO_3 ($E_{\text{max}}=500 \text{ kV cm}^{-1}$)²⁸.

Outlook

Targeted chemical pressure provides a chemical pathway to surpass the conventional limitations imposed on strain-engineered films

by epitaxial strain. Here we show how the $(\text{SrTiO}_3)_{n-1}(\text{BaTiO}_3)_1\text{SrO}$ Ruddlesden–Popper series provides a model for future optimization of complex artificial materials and for advanced growth methods to synthesize high-performance voltage-tunable dielectrics that are viable for application in adaptive and reconfigurable electronics at millimetre-wave frequencies. Single layers of BaTiO_3 were incorporated into $(\text{SrTiO}_3)_n\text{SrO}$ Ruddlesden–Popper superlattices to allow these films to be grown to arbitrary thickness (with proper barium content for the substrate used) with properties enhanced beyond what can be achieved by bulk chemical pressure. The resulting tunable millimetre-wave devices exhibit a 200% improvement in the relevant FOM at 110 GHz compared to the previous best material, $(\text{SrTiO}_3)_n\text{SrO}$ with $n=6$ commensurately strained to (110) DyScO_3 . Future work will examine improvements to film thickness to increase attainable device tuning, as well as film growth on a wider variety of commercially relevant substrates.

Online content

Any methods, additional references, Nature Research reporting summaries, source data, extended data, supplementary information, acknowledgements, peer review information; details of author contributions and competing interests; and statements of data and code availability are available at <https://doi.org/10.1038/s41563-019-0564-4>.

Received: 22 February 2019; Accepted: 12 November 2019;

Published online: 23 December 2019

References

1. Tagantsev, A. K., Sherman, V. O., Astafiev, K. F., Venkatesh, J. & Setter, N. Ferroelectric materials for microwave tunable applications. *J. Electroceram.* **11**, 5–66 (2003).
2. Bao, P., Jackson, T. J., Wang, X. & Lancaster, M. J. Barium strontium titanate thin film varactors for room temperature microwave device applications. *J. Phys. D* **41**, 063001 (2008).
3. Gevorgian, S. *Ferroelectrics in Microwave Devices, Circuits and Systems: Physics, Modeling, Fabrication and Measurements* (Springer, 2009).
4. Subramanyam, G. et al. Challenges and opportunities for multi-functional oxide thin films for voltage tunable radio frequency/microwave components. *J. Appl. Phys.* **114**, 191301 (2013).
5. Meyers, C. J. G., Freeze, C. R., Stemmer, S. & York, R. A. $(\text{Ba},\text{Sr})\text{TiO}_3$ tunable capacitors with RF commutation quality factors exceeding 6000. *Appl. Phys. Lett.* **109**, 112902 (2016).
6. Vorobiev, A., Rundqvist, P., Khamchane, K. & Gevorgian, S. Microwave loss mechanisms in $\text{Ba}_{0.2}\text{Sr}_{0.75}\text{TiO}_3$ thin film varactors. *J. Appl. Phys.* **96**, 4642–4649 (2004).
7. Lee, C.-H. et al. Exploiting dimensionality and defect mitigation to create tunable microwave dielectrics. *Nature* **502**, 532–536 (2013).
8. Ruddlesden, S. N. & Popper, P. New compounds of the K_2NIF_4 type. *Acta Crystallogr.* **10**, 538–539 (1957).
9. Ruddlesden, S. N. & Popper, P. The compound $\text{Sr}_3\text{Ti}_2\text{O}_7$ and its structure. *Acta Crystallogr.* **11**, 54–55 (1958).
10. Tilley, R. J. D. Correlation between dielectric constant and defect structure of non-stoichiometric solids. *Nature* **269**, 229–231 (1977).
11. Tilley, R. J. D. An electron microscope study of perovskite-related oxides in the Sr-Ti-O system. *J. Solid State Chem.* **21**, 293–301 (1977).
12. Knott, L. J., Cockcroft, N. J. & Wright, J. C. Site-selective spectroscopy of erbium-doped SrTiO_3 , Sr_2TiO_4 , and $\text{Sr}_3\text{Ti}_2\text{O}_7$. *Phys. Rev. B* **51**, 5649–5658 (1995).
13. Choi, K. J. et al. Enhancement of ferroelectricity in strained BaTiO_3 thin films. *Science* **306**, 1005–1009 (2004).
14. Béa, H. et al. Evidence for room-temperature multiferroicity in a compound with a giant axial ratio. *Phys. Rev. Lett.* **102**, 217603 (2009).
15. Haislmaier, R. C. et al. Unleashing strain induced ferroelectricity in complex oxide thin films via precise stoichiometry control. *Adv. Funct. Mater.* **26**, 7271–7279 (2016).
16. Wei, Y. et al. A rhombohedral ferroelectric phase in epitaxially strained $\text{Hf}_{0.5}\text{Zr}_{0.5}\text{O}_2$ thin films. *Nat. Mater.* **17**, 1095–1100 (2018).
17. Wood, C. E. C., Metze, G., Berry, J. & Eastman, L. F. Complex free-carrier profile synthesis by “atomic-plane” doping of MBE GaAs. *J. Appl. Phys.* **51**, 383–387 (1980).
18. Schubert, E. F. Delta doping of III–V compound semiconductors: Fundamentals and device applications. *J. Vac. Sci. Technol. A* **8**, 2980–2996 (1990).
19. Birol, T., Benedek, N. A. & Fennie, C. J. Interface control of emergent ferroic order in Ruddlesden–Popper $\text{Sr}_{n+1}\text{Ti}_n\text{O}_{3n+1}$. *Phys. Rev. Lett.* **107**, 257602 (2011).
20. Neaton, J. B. & Rabe, K. M. Theory of polarization enhancement in epitaxial $\text{BaTiO}_3/\text{SrTiO}_3$ superlattices. *Appl. Phys. Lett.* **82**, 1586–1588 (2003).
21. Tenne, D. A. et al. Probing nanoscale ferroelectricity by ultraviolet Raman spectroscopy. *Science* **313**, 1614–1616 (2006).
22. Bland, J. A. The crystal structure of barium orthotitanate, Ba_2TiO_4 . *Acta Crystallogr.* **14**, 875–881 (1961).
23. Lee, S., Randall, C. A. & Liu, Z.-K. Modified phase diagram for the barium oxide–titanium dioxide system for the ferroelectric barium titanate. *J. Am. Ceram. Soc.* **90**, 2589–2594 (2007).
24. Kwestroo, W. & Paping, H. A. M. The systems $\text{BaO}-\text{SrO}-\text{TiO}_2$, $\text{BaO}-\text{CaO}-\text{TiO}_2$, and $\text{SrO}-\text{CaO}-\text{TiO}_2$. *J. Am. Ceram. Soc.* **42**, 292–299 (1959).
25. Veličkov, B., Kahlenberg, V., Bertram, R. & Bernhagen, M. Crystal chemistry of GdScO_3 , DyScO_3 , SmScO_3 , and NdScO_3 . *Z. Für. Krist.* **222**, 466–473 (2007).
26. Xi, X. X. et al. Oxide thin films for tunable microwave devices. *J. Electroceram.* **4**, 393–405 (2000).
27. Houzet, G., Burgnies, L., Velu, G., Carru, J.-C. & Lippens, D. Dispersion and loss of ferroelectric $\text{Ba}_{0.5}\text{Sr}_{0.5}\text{TiO}_3$ thin films up to 110 GHz. *Appl. Phys. Lett.* **93**, 053507 (2008).
28. Gu, Z. et al. Resonant domain-wall-enhanced tunable microwave ferroelectrics. *Nature* **560**, 622–627 (2018).

Publisher's note Springer Nature remains neutral with regard to jurisdictional claims in published maps and institutional affiliations.

© The Author(s), under exclusive licence to Springer Nature Limited 2019

Methods

Oxide MBE growth. The $n=2-6$ (SrTiO_3) _{$n-1$} (BaTiO_3)₁ n SrO phases were grown using a Veeco GEN10 oxide MBE system at 875 °C (as measured by the substrate heater thermocouple) in an oxygen with 10% ozone background pressure of 1.3×10^{-4} Pa (1×10^{-6} Torr). Films with periodicity index $n=2-6$ were grown to a thickness of ~ 50 nm on (110) DyScO_3 substrates ($a_{\text{pseudocubic}} \approx 3.949 \text{ \AA}$)²⁵, while an additional film of thickness 100 nm was grown for the $n=6$ structure. Atomic layering was achieved by elemental source shuttering and careful calibration of individual SrO, TiO_2 and BaO monolayer shutter times using reflection high-energy electron diffraction intensity oscillations^{29,30}.

Dielectric measurements as a function of temperature. Interdigitated capacitors (IDCs) were photolithographically patterned on the 50-nm $n=2-6$ (SrTiO_3) _{$n-1$} (BaTiO_3)₁ n SrO thin films grown on (110) DyScO_3 using thermally evaporated electrodes, 100 nm of gold on a 10-nm chromium adhesion layer. The IDC array contains electrodes with finger lengths of 500 μm , finger widths of 5 μm , with finger gaps 6, 10 and 15 μm and the number of fingers 34, 24 or 20, respectively. An LCR meter coupled with a cryogenic measurement station cooled with liquid helium was used to measure capacitance and resistance of the IDC as a function of temperature. The capacitance and resistance were converted to the dielectric constant and loss using the techniques described in refs. ^{31,32}. For each sample one IDC device was measured at all temperatures. At room temperature, a sample's complete array of IDC devices was measured and averaged to correct the curve of the single device measured with temperature. The standard deviation of the room-temperature dielectric constant across a sample's whole IDC array varied from 9 to 32% depending on the quality of the sample's photolithographic patterning. Ferroelectric measurements shown in Supplementary Fig. 7a were measured with the same cryogenic station and IDC structures, by use of a commercial ferroelectric tester.

Summary of first-principles calculations. All calculations were performed with the Vienna Ab-initio Software Package (VASP, v.5.4.1)^{33,34}, which implements the projector-augmented wave (PAW) formalism of DFT. We used the PBEsol exchange-correlation functional³⁵ (Perdew–Burke–Ernzerhof revised for solids) and PAW potentials, and valence electron configurations Sr sv ($4s^2 4p^6 5s^2$), Ba sv ($5s^2 5p^6 6s^2$), Ti sv ($3p^6 4s^2 3d^1$) and O sv ($2s^2 2p^4$) from the standard VASP potential library. Wave functions were expanded in plane waves up to an energy cutoff of 550 eV. We used conventional unit cells (two formula units) in the calculations, and the Brillouin zone was sampled on a Monkhorst–Pack grid³⁶ of $8 \times 8 \times N_z$ k-points, where $N_z=4$ for the $n=1$ (SrTiO_3) _{$n-1$} (BaTiO_3)₁ n O Ruddlesden–Popper structure; $N_z=2$ for $n=2$ and 3 and $N_z=1$ for $n \geq 4$.

Following earlier theoretical work on SrTiO_3 -based Ruddlesden–Popper dielectrics^{7,19}, we simulated epitaxial growth on (110) DyScO_3 by fixing the in-plane lattice parameter of the Ruddlesden–Popper structures to 3.9386 \AA , which is 1.1% larger than the theoretical (PBEsol) lattice parameter for SrTiO_3 (3.8958 \AA). The structures were relaxed keeping the lattice parameters fixed in the *ab* plane, while the *c* lattice parameter and all internal coordinates were allowed to relax until the Hellmann–Feynman forces on all atoms were below 0.1 meV \AA^{-1} .

Phonon calculations were done with Phonopy³⁷, which implements the finite displacement method to calculate the force constant matrix. Only phonons at the Brillouin zone centre (Γ) were considered. Polar ground states were obtained from the aristotype *I4/mmm* structures by freezing in the phonon eigenvectors corresponding to unstable modes³⁸, and relaxing the structures under conditions of fixed biaxial strain. The relevant ferroelectric instability is a doubly degenerate polar phonon of E_u symmetry, and the ground state structure with space group symmetry *F2mm* is found for polarization along [110] (ref. ³⁹).

Figures of the crystal structures were created with VESTA (visualization for electronic and structural analysis)⁴⁰.

Millimetre-wave device fabrication and measurement. The broadband dielectric properties of the 100-nm-thick $n=6$ thin-film sample were determined over a frequency range from 600 Hz to 110 GHz, through complex scattering (S) parameter measurements of various planar microelectronic circuit devices patterned directly on the surface of the thin-film sample chip. The circuit devices were patterned via mask-less ultraviolet photolithography followed by electron-beam evaporation of a 10-nm titanium adhesion layer and a 500-nm gold electrode layer. The individual devices were completed with a lift-off step, to remove the excess metal and remaining photoresist, followed by a gentle cleaning in standard solvents and a light oxygen plasma.

Below 100 MHz, the S parameters of a series of four interdigitated capacitors (IDCs) with active lengths ranging from 0.210 to 2.910 mm were measured and used to determine the admittance per unit length of the IDC structures. IDC cross-sections comprised three 20- μm -wide fingers, separated by 5- μm -wide gaps, as well as 200- μm -wide ground planes, spaced 20 μm away from the outer fingers of the IDCs (Supplementary Fig. 8a). The IDC measurements were performed with two different instruments: an LCR meter (600 Hz to 1 MHz) and a radiofrequency vector network analyser (RF VNA, 500 kHz to 200 MHz). The LCR meter was calibrated with a built-in two-standard Open–Short calibration, while the RF VNA was calibrated by on-wafer Open–Short–Load–Thru standards. From 100 MHz to 110 GHz, the complex S parameters of the coplanar waveguide (CPW) devices were

measured with a microwave-frequency VNA. The CPW cross-section consisted of a 20- μm -wide centre conductor, a 5- μm -wide gap and a 200- μm -wide ground plane (Supplementary Fig. 8b). The thin-film chip contained seven transmission lines with active lengths ranging from 0.420 to 7.500 mm. Line lengths were optimized to reduce uncertainty when applying the multiline through-reflect-line (multiline-TRL) calibration⁴¹. A total of three chips are needed to complete a full measurement: the thin-film chip with the film deposited on (110) DyScO_3 substrate, a bare companion (110) DyScO_3 substrate (shown in Supplementary Fig. 8c) and a custom reference calibration chip with standards that are geometrically similar to the devices on the sample and substrate chips.

Measurements were conducted on a temperature-controlled stage, and devices were contacted by ground–signal–ground microwave probes mounted on micro-positioners. In this case, the reference chip contained similar CPW and IDC devices patterned on a (001) LaAlO_3 substrate. An additional 12-nm PdAu layer was deposited on the reference chip to produce resistor standards. Series resistor standards were used alongside a series capacitor, symmetric reflect and all CPW lines to perform the full calibration procedure, which consistently defines the reference impedance over the full experimental frequency range. The calibration consists of two tiers. In the first tier, a multiline-TRL-based calibration was performed using the NIST StatistiCal software package, which implements an optimization algorithm to produce an estimate for γ_0 , the propagation constant of the transmission lines on the reference chip⁴². The propagation constant is defined in terms of the transmission-line distributed circuit parameters as $\gamma_0 = \sqrt{R + i\omega L} \sqrt{G + i\omega C}$, where R , L , C and G are the distributed resistance, inductance, capacitance and conductance per unit length, respectively, and ω is the angular frequency. A low-loss reference calibration substrate was chosen to produce reference transmission lines with a constant C and negligible G in the measured frequency range. The multiline-TRL calibration was compared with a subsequent series resistor calibration to provide an estimate for C for the transmission lines on the reference chip, which is required to extract R and L to describe the frequency-dependent response of the Au conductors^{34,44}. The first-tier calibration produced error correction matrices that account for signal attenuation and phase shift in the network analysers and cables, and other systematic effects such as reflection at connector interfaces, and produced S parameters corrected to 50- Ω characteristic impedance with reference planes located at the probe tips. In the second tier, all transmission lines and a reflect standard were measured on both the companion DyScO_3 chip and the thin-film chip, and corrected with the error matrices from the first-tier calibration. The multiline-TRL algorithm was again used to determine the propagation constant of the transmission lines on the substrate and thin-film chips, as well as to estimate the characteristic impedance of these transmission lines. The resulting propagation constants for the companion substrate chip and the thin-film chip were further analysed with the aid of finite-element modelling to determine the broadband dielectric properties.

Device dimensions were measured via optical microscopy and surface profilometry and were used to generate two-dimensional simulations of the electromagnetic field distributions by means of a two-dimensional finite-element modelling package. First, the R and L terms were calculated as a function of frequency, based on estimates of the DC conductivity, and the model was validated by comparing to an R and L determined via the circuit parameter extraction approach mentioned above^{42,43}. The simulated R and L were then used to extract the frequency-dependent C and G from the measured propagation constant. The two-dimensional simulations were used again to develop a mapping function that relates the measured frequency-dependent capacitance and conductance to the real (K'_{11}) and imaginary (K''_{11}) parts of the in-plane complex permittivity, respectively. External bias tees were used to apply a DC bias voltage to the CPW structures up to 200 V, over the frequency range from 100 MHz to 40 GHz, corresponding to a maximum applied field of $E_{\text{max}} = 400 \text{ kV cm}^{-1}$. Complex S parameters were measured with a microwave-frequency VNA at applied electric field bias points stepped in 5 kV cm^{-1} increments. The software used to implement the multiline-TRL calibration also provided 95% confidence interval estimates for the effective permittivity (and hence for the propagation constant) at each frequency point. These uncertainties were propagated through the analysis to determine the corresponding relative uncertainty in the measurements of the dielectric permittivity (Supplementary Fig. 9a).

Data availability

Figure data, DFT files and additional information can be accessed on the NIST Public Data Repository via the following link: <https://doi.org/10.18434/M31968>.

References

29. Haeni, J. H., Theis, C. D. & Schlom, D. G. RHEED intensity oscillations for the stoichiometric growth of SrTiO_3 thin films by reactive molecular beam epitaxy. *J. Electroceram.* **4**, 385–391 (2000).
30. Haislmaier, R. C., Stone, G., Alem, N. & Engel-Herbert, R. Creating Ruddlesden–Popper phases by hybrid molecular beam epitaxy. *Appl. Phys. Lett.* **109**, 043102 (2016).
31. Gevorgian, S. S., Martinsson, T., Linner, P. L. J. & Kollberg, E. L. CAD models for multilayered substrate interdigital capacitors. *IEEE Trans. Microw. Theory Tech.* **44**, 896–904 (1996).

32. Kidner, N. J., Homrighaus, Z. J., Mason, T. O. & Garboczi, E. J. Modeling interdigital electrode structures for the dielectric characterization of electroceramic thin films. *Thin Solid Films* **496**, 539–545 (2006).
33. Kresse, G. & Furthmüller, J. Efficient iterative schemes for ab initio total-energy calculations using a plane-wave basis set. *Phys. Rev. B* **54**, 11169–11186 (1996).
34. Kresse, G. & Joubert, D. From ultrasoft pseudopotentials to the projector augmented-wave method. *Phys. Rev. B* **59**, 1758–1775 (1999).
35. Perdew, J. P. et al. Restoring the density-gradient expansion for exchange in solids and surfaces. *Phys. Rev. Lett.* **100**, 136406–136406 (2008).
36. Monkhorst, H. J. & Pack, J. D. Special points for Brillouin-zone integrations. *Phys. Rev. B* **13**, 5188–5192 (1976).
37. Togo, A. & Tanaka, I. First principles phonon calculations in materials science. *Scri. Mater.* **108**, 1–5 (2015).
38. Togo, A. & Tanaka, I. Evolution of crystal structures in metallic elements. *Phys. Rev. B* **87**, 184104 (2013).
39. Stokes, H. T., Hatch, D. M. & Campbell, B. J. *ISOTROPY Software Suite* (Brigham Young University, 2015); <https://stokes.byu.edu/iso/isotropy.php>
40. Momma, K. & Izumi, F. VESTA 3 for three-dimensional visualization of crystal, volumetric and morphological data. *J. Appl. Crystallogr.* **44**, 1272–1276 (2011).
41. Marks, R. B. A multiline method of network analyzer calibration. *IEEE Trans. Microw. Theory Tech.* **39**, 1205–1215 (1991).
42. Williams, D. F., Wang, J. C. M. & Arz, U. An optimal vector-network analyzer calibration algorithm. *IEEE Trans. Microw. Theory Tech.* **51**, 2391–2401 (2003).
43. Williams, D. F., Marks, R. B. & Davidson, A. Comparison of on-wafer calibrations. In *Proc. 38th Automatic RF Techniques Group Conference Dig* 68–81 (IEEE, 1991).
44. Orloff, N. D. et al. A compact variable-temperature broadband series-resistor calibration. *IEEE Trans. Microw. Theory Tech.* **59**, 188–195 (2011).

Acknowledgements

The synthesis, characterization and theoretical work at Cornell was supported by the US Department of Energy, Office of Basic Sciences, Division of Materials Sciences and

Engineering (Award no. DE-SC0002334). Sample preparation was in part facilitated by the Cornell NanoScale Facility, a member of the National Nanotechnology Coordinated Infrastructure (NNCI), which is supported by the National Science Foundation (grant no. NNCI-1542081). Ferroelectric and dielectric measurements with temperature were conducted at the Center for Nanophase Materials Sciences, which is a DOE Office of Science User Facility. Infrared and terahertz studies were supported by the Czech Science Foundation (project no. 18–09265S) and by the MŠMT (project no. SOLID21-CZ.02.1.01/0.0/0.0/16 019/0000760). This work made use of Cornell Center for Materials Research Shared Facilities, which are supported through the NSF MRSEC program (no. DMR-1719875). Certain commercial equipment, instruments or materials are identified in this article to specify the experimental procedure adequately. Usage of commercial products herein is for information only; it does not imply recommendation or endorsement by NIST, and it is not intended to imply that the materials or equipment identified are necessarily the best available for the purpose.

Author contributions

N.M.D. and J.Z. synthesized the samples under the supervision of D.G.S. N.M.D. performed the ferroelectric and low frequency dielectric measurements versus temperature. G.H.O. performed the DFT calculations under the supervision of C.J.E. M.E.H. performed STEM measurements under the supervision of D.A.M. Millimetre-wave devices were fabricated and measured by E.J.M., A.M.H., X.L. and J.A.D. under the supervision of C.J.L., J.C.B. and N.D.O. R.U. and S.G. supplied the DyScO₃ substrates. V.G. and C.K. performed the infrared and terahertz measurements under the supervision of S.K. N.M.D. D.G.S. E.J.M., A.M.H., N.D.O., G.H.O and M.E.H. wrote the manuscript. All authors discussed results and commented on the manuscript. The study was conceived and guided by D.G.S.

Additional information

Supplementary information is available for this paper at <https://doi.org/10.1038/s41563-019-0564-4>.

Correspondence and requests for materials should be addressed to D.G.S.

Reprints and permissions information is available at www.nature.com/reprints.